Characterization of Widefield THz Optics Using Phase Shifting Interferometry

Reyes, Nicolás; Mayorga, Ivan Cámara; Grutzeck, Gerrit; Yates, Stephen J.C.; Baryshev, Andrey; Baselmans, Jochem; Weiss, Axel; Klein, Bernd

DOI
10.1109/TTHZ.2023.3320554

Publication date
2023

Document Version
Final published version

Published in
IEEE Transactions on Terahertz Science and Technology

Characterization of Widefield THz Optics Using Phase Shifting Interferometry

Nicolás Reyes, Ivan Cámara Mayorga, Gerrit Grutzeck, Stephen J.C. Yates, Andrey Baryshev, Jochem Baselmans, Axel Weiss, and Bernd Klein

***Abstract*—Characterization of wide-field optics in the Terahertz regime imposes new and demanding requirements for testing systems. Basic optical parameters can be determined from scalar planar characterization, obtained using monochromatic or thermal sources located in the instrument focal plane. In contrast, important features, such as the spillover efficiency, wave front error, or aperture efficiency cannot be easily measured by such approaches. Moreover, when instruments have a curved focal plane, designed to match the hosting telescope, even basic parameters are difficult to extract from scalar planar measurements. In such cases, the use of phase and amplitude information is mandatory. From a complex planar measurement, the complete information of the optical system can be obtained, allowing the estimation of all relevant optical parameters. In this work, we present and demonstrate experimentally a technique to perform such measurement based on the use of continuous wave photonic terahertz sources. Here, we present our results at 350 GHz and 850 GHz, demonstrating the feasibility of performing measurements at different submillimeter frequencies using a single experimental setup. The proposed system was implemented to fully characterize a wide-field submillimeter camera based on kinetic inductance detectors designed to be deployed at the APEX Telescope in Chile.**

***Index Terms*—Experimental methods, kinetic inductance detectors, terahertz optics.**

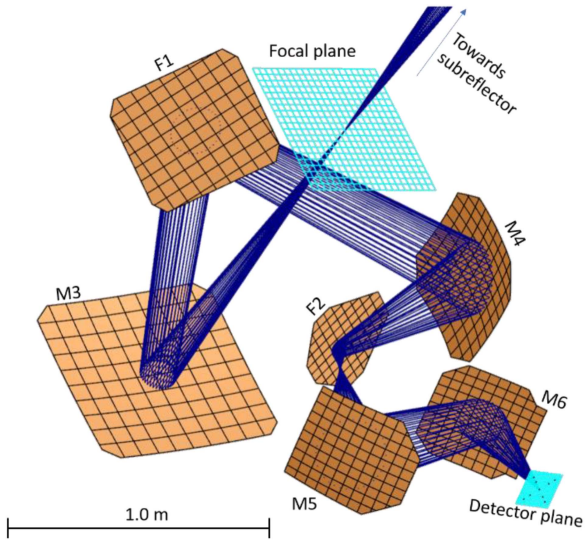

Fig. 1. Schematic of the A-MKID optic system. It consists of 6 reflective mirrors, which have an overall magnification of 3.6. In the figure, the optical rays of the central pixel are shown.

I. Introduction

THERE is an urgent demand for instruments in the submillimeter range consisting of large array detectors with wide field of view and high mapping speed [1], [2]. Microwave kinetic inductance detector (MKID) [3] technology is ideally suited to meeting these requirements, as every pixel possess resonant circuits with a high-quality factor, enabling frequency domain multiplexing up to thousand pixels per array [4]. In addition, the fabrication process employs conventional, optical and electron beam, lithography, and the achieved photon noise limited sensitivity is given by the full instrument optical efficiency and optical loading [5], in the atmospheric loading limit for ground-based astronomy. MKID technology has been successfully deployed in the NIKA-2 [6] experiment, and is to be used in many future planned and in development instruments such as [7], [8], [9], and [2]. The A-MKID instrument is a dual-color bolometer camera, operating at 350 GHz and at 850 GHz simultaneously. It is designed to be deployed at the 12 m APEX telescope in Chile [10], a location that offer excellent observation conditions in the submillimeter wavelength range. The two operating frequencies of the instrument are centered on the atmospheric transmission windows. Both arrays are duplexed in polarization, covering the same 15' × 15' area of the sky. The instrument optic has a magnification of 3.6, required to transform the detector plane into the telescope focal plane. Design beam sizes on sky are 17.1" for the 350 GHz array and 7.5" for 850 GHz. The optical system consists of six reflective mirrors as depicted in Fig. 1. All optic surfaces were defined as extended polynomial expressions and were

Manuscript received 28 April 2023; revised 18 August 2023; accepted 11 September 2023. Date of publication 28 September 2023; date of current version 3 November 2023. *(Corresponding author: Nicolás Reyes.)*

Nicolás Reyes, Ivan Cámara Mayorga, Gerrit Grutzeck, Axel Weiss, and Bernd Klein are with the Max Planck Institute for Radio-Astronomy, 53121 Bonn, Germany (e-mail: nreyes@mpifr-bonn.mpg.de; imayorga@mpifr-bonn.mpg.de; ggrutzeck@mpifr-bonn.mpg.de; aweiss@mpifr-bonn.mpg.de; bklein@mpifr-bonn.mpg.de).

Stephen J.C. Yates is with the SRON, Netherland Institute for Space Research, 9747 AD Groningen, The Netherlands (e-mail: s.yates@sron.nl).

Andrey Baryshev is with the Kapteyn Astronomical Institute, University of Groningen, 9712 CP Groningen, The Netherlands, and also with the Max Planck Institute for Radio-Astronomy, 53121 Bonn, Germany (e-mail: andrey@astro.rug.nl).

Jochem Baselmans is with the SRON, Netherland Institute for Space Research, 2333 Leiden, The Netherlands, and also with the Faculty of Electrical Engineering, Mathematics, and Computer Science, Department of Microelectronics, Delft University, 2628 Delft, The Netherlands (e-mail: j.baselmans@sron.nl).

Color versions of one or more figures in this article are available at https://doi.org/10.1109/TTHZ.2023.3320554.

Digital Object Identifier 10.1109/TTHZ.2023.3320554

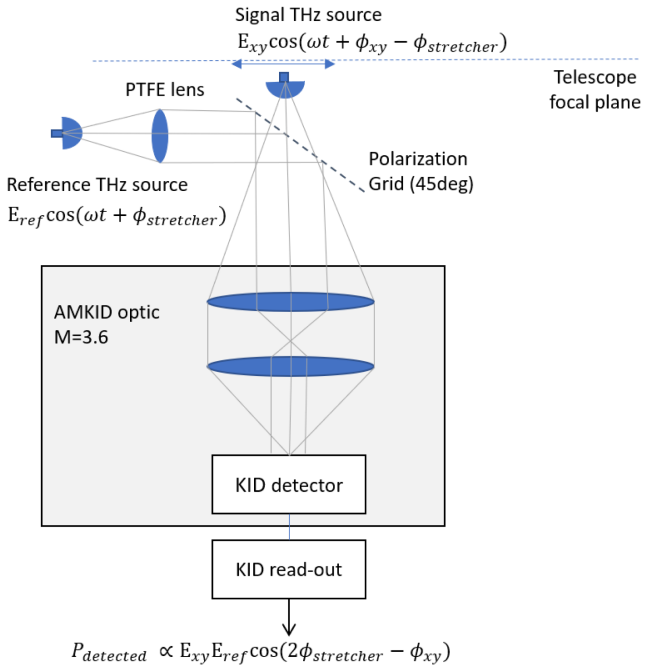

Fig. 2. Schematic of the experimental setup. Reference and signal sources are generated at the instrument focal plane. Both signals propagate through the optics and are detected by the KID detector.

optimized to achieve a diffraction limited performance, with a Strehl ratio better than 0.8 over the complete field of view [11].

Before the instrument deployment, a full characterization of the system optical performance is mandatory. To achieve this goal a phase and amplitude measuring system was implemented. Such systems with MKID arrays have been previously demonstrated by [12], [13], and [14], a heterodyne technique, using the interference beat between two frequency offset solid-state multiplier sources with a common phase reference. In this work, we present a novel implementation of a phase and amplitude beam measuring system based in the use of terahertz photonic sources and phase shifting interferometry. This approach has the advantage of allowing for fast phase modulation, smaller size and weight and, the largest advantage, the ability to switch in frequency over a large frequency range, covering almost the complete submillimeter spectra, from 100 GHz up to 2 THz. This feature is especially convenient in our case, as it allows for a direct characterization of the two frequency bands included in the system under study.

II. Experimental Setup

The experimental setup implemented in our laboratory is represented in Fig. 2. It consists of two terahertz sources located at the instrument focal plane. Both sources radiate at the same frequency, but the relative phase between them is controlled via optical fiber stretchers. The designed system uses the interference between these two sources to measure the instrument complex beam pattern. The signal source is mounted on a XY translation stage, whereas the reference source is static and couples to the detectors via a polarization grid. To achieve the best possible resolution and avoid convolution effects, the signal source must be as similar as possible to a point source at focal plane. For this purpose, the signal source is mounted behind a small aperture (3 mm diameter) on a large absorber plate. The size of the aperture and the polarization angle were carefully adjusted to ensure that at maximum signal level the detectors do not saturate. The large absorber sheet also minimizes thermal background variations during the scan, whilst keeping the system in linear regime.

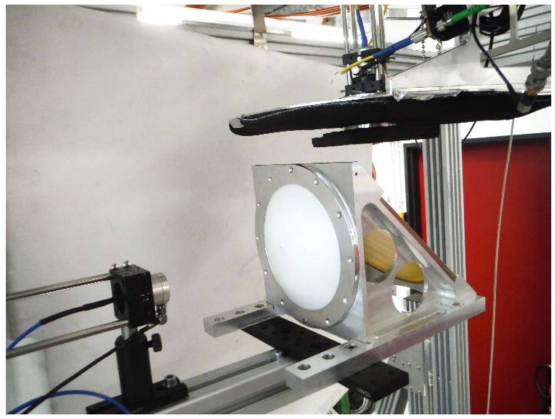

Fig. 3. Image of the two terahertz sources located at the focal plane of the instrument. The reference source PTFE lens is clearly visible along with the polarization grid.

On other hand, the reference optics must ideally illuminate the complete scan area and, therefore, some additional optics is needed. This was done by using a 10 cm PTFE lens with a focal length of 12 cm. The photonic device acting as the reference source was modified to obtain a half power beam width of 30° instead of the original 7.1° (values at 350 GHz). With this modification, we enlarge the illuminated area whilst keeping a compact size for the associated optics. Fig. 3 shows a photography of the described configuration. The illumination of the focal plane by the reference source, along with the size of the combining grid set the maximum scan range of the system. In our setup, this limitation results in a maximum scan area of 10×10 cm^2.

The two generated signals are controlled in phase using fiber stretchers. KID detectors are linearly polarized, and react to the instantaneous power reaching the device. This power is proportional to the squared electric field at the detector, corresponding to the addition of the fields generated by the two photonic sources. The signal generated by these can be described as

$$\overrightarrow{E}_{\text{reference}} = E_{ref}\cos\left(wt + \phi_{\text{stretcher}}\right)\hat{x} \tag{1}$$

$$\overrightarrow{E}_{\text{signal}} = E_{xy}\cos\left(wt + \phi_{xy} - \phi_{\text{stretcher}}\right)\hat{x} \tag{2}$$

where $\hat{x}$ is aligned with detector polarization direction, E_{ref} is the amplitude of the reference, and E_{xy} is the amplitude of the main signal, which depend on the xy position. It is important to note that the reference source is static, and its phase term just depends on the stretcher induced phase $\phi_{\text{stretcher}}$. In contrast to this, the signal source phase term has two components: one induced

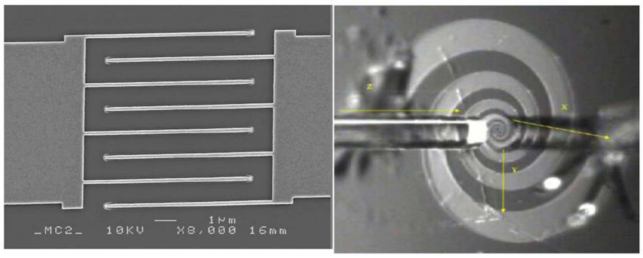

Fig. 4. (Left) SEM picture for the active area of the photomixing element. (Rigth) Photomixer illuminated by fiber optics. A planar log-spiral antenna is fed by the photomixer active area.

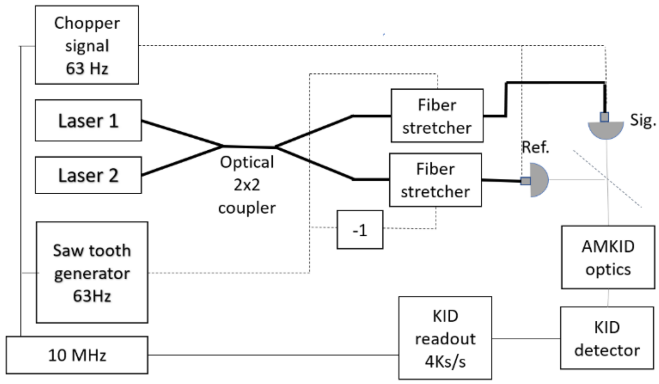

Fig. 5. Electronic diagram of our test setup. The two photomixers are driven by two lasers optically combined in an optical 2×2 coupler. Stretchers provide phase control on the generated signals. A ramp generator is used to drive the stretchers, whereas an electronic chopper is used for synchronization of interferograms. All relevant devices are phase locked to the same reference. The output of the detector is sampled by the KID readout.

by the stretcher and the second one depending on the *xy* position of the source. We refer to this term as ϕ_{xy}. The interference of the two terahertz signals propagates through the AMKID optical system and reaches the detectors. The signal is modulated by varying the phase between the sources, reference and signal. As the two signals interfere in the detector, a modulation signal is generated. The detected signal by our KID readout is

$$P_{\text{detected}} = k * E_{xy} \cos\left(2 * \phi_{\text{stretcher}} - \phi_{xy}\right) \tag{3}$$

where k is a constant representing all static components in the system, as the amplitude of the reference E_{ref}. As previously described, E_{xy} and ϕ_{xy} are the amplitude and phase of the beam pattern, which depend on the scanner position. To retrieve them from the measurement a linear phase modulation is introduced. For every period of the phase modulation an output signal of the form

$$P_{\text{detected}} = k * E_{xy} \cos\left(\alpha t - \phi_{xy}\right) \tag{4}$$

is obtained. From there the extraction of E_{xy} and ϕ_{xy} is straightforward. Note the detected signal power is proportional to E_{xy}, the E-field amplitude, so increasing signal to noise by the power of two compared to amplitude only "thermal source" measurement used traditionally for sub-mm direct detectors [15].

III. Photonic System

A key aspect of our system is the use of photomixers as sources of terahertz radiation. A photomixer is an optoelectronic device designed for optical heterodyning, i.e., for the generation of a beat-note from the interference of two optical monochromatic signals -near infrared (NIR) lasers in our case-, impinging on a biased semiconductor material. This material is engineered to absorb the optical power generating electron-hole pairs. These are separated by the electric field between two biased electrodes [see Fig. 4(a)], thereby creating a photocurrent proportional to the optical intensity and the bias electric field. The ultrashort electron lifetimes of the photomixer material, allows the photocurrent to "follow" the envelope of the optical instantaneous power, which contains the laser difference frequency component. Therefore, the tunability of commercially available NIR lasers translates directly into the wide frequency span of the emitted signal. The photomixer active area feeds a radiating element. In our device, a broadband spiral antenna [see Fig. 4(b)], emitting from few GHz to several THz is used. Finally, the devices include an extended hemispherical silicon lens glued over the radiating element. The lens collimates the beam and couple it to free space. Device power output is proportional to the square of bias voltage and laser power. In addition, the terahertz power decreases with frequency by 6 dB/oct beyond each cut-off frequency (typically about 500 GHz and 1.5 THz, corresponding to the carrier lifetime and *RC* constant, respectively). Devices used in this work had been extensively described in [16] and [17]. Current devices generate several hundred of nW of power at 850 GHz. This power is more than sufficient to run our experiment and the power level was carefully adjusted to avoid detector saturation. The device output beam size is also depending on frequency and has a half power beam width of 7.1° at 350 GHz and 5.5° at 850 GHz. In our experimental setup, depicted in Fig. 5, we use two photomixers as terahertz sources. They are driven by the same laser references: two single mode, narrow linewidth, 780 nm lasers combined in a polarization maintaining fiber coupler. The free-running lasers are temperature stabilized, yielding a typical frequency drift of around 10 MHz. When the interfering arms of the reference and main signal differ in length, the frequency drift translates into a phase drift according to

$$\Delta\phi = \frac{2\pi}{c} * f_{\text{drift}} * \Delta_{\text{length}} \tag{5}$$

where c is the speed of light, f_{drift} the drift between lasers, and Δ_{length} the difference in length between the two optical paths.

Our setup is conceived having a difference of interfering arms of less than 1 m leading to a phase drift of about 10°. This noise is a "fast" variation and average to zero during data acquisition. In addition, the system, based on photonic reference signals distributed via optic fibers, provide an excellent terahertz signal phase stability of few degrees over several hours. The phase control was implemented by using two fiber stretchers, one per photomixer. Both stretchers are driven by saw-teeth signals with opposite voltages, achieving a total phase delay between lines of 1.1 mm when applying a 100 V signal. This length, equivalent to 700° at 350 GHz, has to be adjusted as a function

of the frequency of measurement. By using this symmetric configuration, we cancel out asymmetries in the system, which can lead to systematic errors in the phase measurement.

IV. Phase Shifting Interferometry

Phase shifting interferometry is a well-known technique used for optic surface characterization [18]. The technique consists of using an interferometer in which one of the arms is used to illuminate the surface under study, whilst the other arm is used to generate a linear phase shift. The obtained interferograms between the two arms are captured and subsequently used to retrieve the surface features. As described in previous sections, we use an analogue technique but we introduce the controlled phase shift electronically, using fiber stretchers instead of the traditional mechanic delay lines. Additionally, we aim to test a complex set of reflecting elements instead of a single optical element. Further complexity comes from the need of a multiple frequency system, able to deliver data for our both arrays. In our opinion, the proposed methodology represents an alternative which mitigates the complexity of other measurement based on solid state sources and frequency modulation to generate interference. To better describe the data acquisition and processing the 350 GHz case is presented first. Later, in Section VI, the results obtained with the same system at the higher 850 GHz band are shown.

A. Data Acquisition

Every measuring cycle corresponds to an interferogram. It starts with the saw-teeth signal set to zero volts. During a cycle the ramp voltage increases, driving the stretchers and generating a linear phase shift between the reference and main signals. As the cycle ends the sources are electrically switched OFF by using a chopper signal. During the OFF time the stretchers are reset to the original position and set to be ready for the next cycle. The measurement time was set to around 16 ms (63 Hz).

A duty cycle of 80% allows for a comfortable resetting of the stretchers. The interference between the two signals is captured by our prototype KID read-out, able to sample at frequencies up to 4 K samples/s. This allows high XY scanning speeds and oversampling of phase modulation, relevant features to efficiently obtain Nyquist sampled maps with the desired signal to noise ratio (SNR). An overview of the new read-out technology, as used for this experiment, can be found in [19]. To facilitate data analysis, the sampling frequency was set to be an integer multiple of the cycle frequency (∼63 Hz). It is important to note that all involved signals are phase locked to the same 10 MHz reference, and that some phase adjustments are required for optimal performance. A timeline example and a close up on a single interferogram is shown in Fig. 6(a) and (b). As seen in Fig. 6(c), the phase and beam information can be easily extracted from each interferogram. This can be achieved by fitting a sinusoid to the trace, or, as we did, by a Fourier transform and selection of the relevant component. The deviation from a perfect sinusoid plot can be identified as a third harmonic component of the main sinusoid. This is caused by nonlinear effects in the stretchers. As expected the effect is more relevant at low frequency (350 GHz) as the stretchers require large voltages to achieve the required modulation. The use of two stretchers reduce the effect but we envision a limitation when measuring at frequencies below 100 GHz. This can be easily overcome by using large range stretchers.

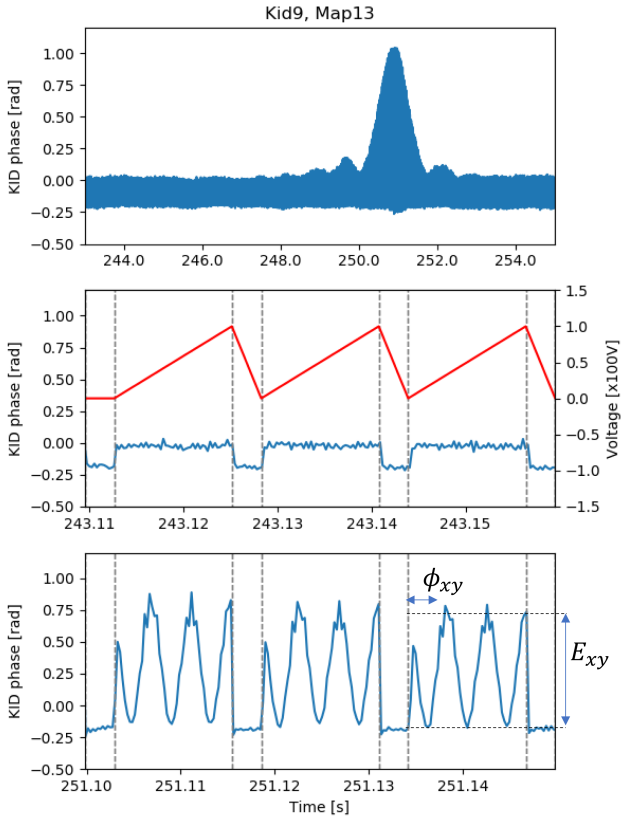

Fig. 6. Top, timeline of the measured KID phase, proportional to the detected power P_{detected} obtained during a line scan. Note that signals are in the linear range (±1 radian). Center, close-up of the stretcher signal (red) and timeline in a position where just the reference signal is present but the interference signal is absent (blue). Dashed lines indicate the ON-OFF times of the sources. Bottom, typical interference pattern between the main signal and reference.

V. Beam Analysis

The data acquisition process runs continuously during the operation of the XY scanners. A velocity of 10 mm/s was set to scan an area of 100 × 100 mm^2 with a 3 mm granularity resolution. The scan is performed line by line. To avoid systematic errors, all lines are scanned in the same direction, thereby allowing a line return at a maximum stage speed, as large as 80 mm/s. It must be highlighted that the KID read-out measures simultaneously all detectors in the read-out line, i.e., around 1000 detectors. Out of these just a subset has relevant information as just a fraction of the array focal plane is scanned using our single read-out chain. For a single scan around 50 GB of raw data are collected. The first step in the data analysis is to identify the pixels with sufficient signal level. For this purpose, the presence of the chopper signal is used. Selected timelines in which a signal is detected are stored for further processing. The selected timelines are analyzed as described in previous section to retrieve the phase and amplitude

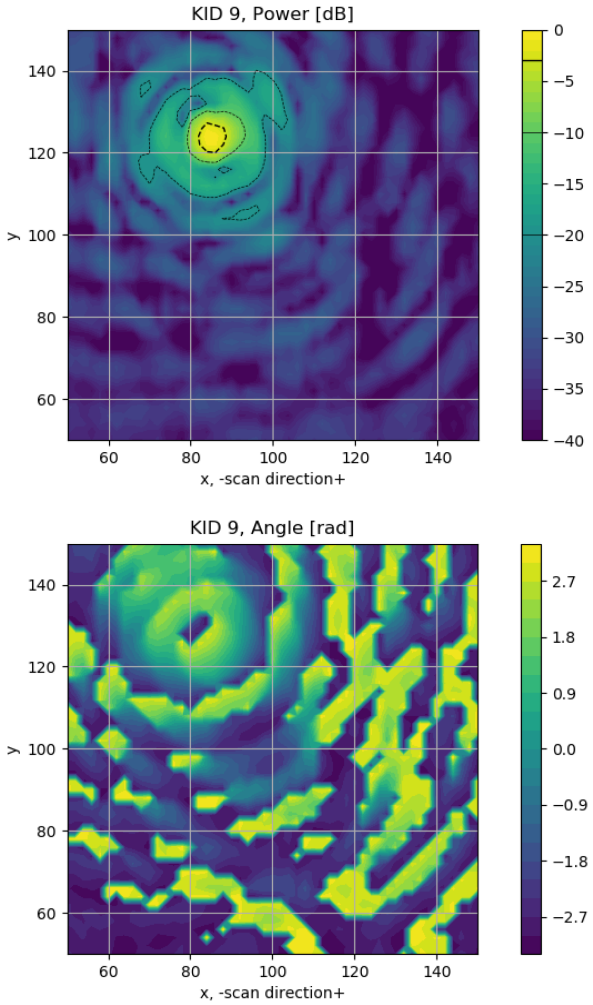

Fig. 7. Amplitude (top) and phase (bottom) beam map of a specific detector in the sampled area. Along with the showed pattern around 30 more good quality maps (SNR $>$ 20 dB) are obtained in the scanned area.

information. The obtained data is combined with the XY scanner positions. From this dataset the complex beam patterns can be obtained, as presented in Fig. 7, which shows a typical KID beam map measured at 350 GHz.

For each scan covering a 10 $\times$ 10 cm^2 area, a set of around 100 beam maps with a signal to noise ratio better than 20 dB are typically measured. The main limiting factor turned out to be the reference signal, which does not fully illuminate the scanned area. Currently a new optical setup to magnify the illumination area of the reference beam is being developed, which will allow to scan larger areas with better illumination.

Post processing using Fourier optics, similar to the process proposed in [15] allows the calculation of important optical parameters such as spillover efficiency, wave front distortion, and aperture efficiency. The first step is to calculate the electric field distribution at the telescope secondary and power normalize it. As the secondary mirror is located 6 m from the measurement plane and since the beam sizes are of the order of 10 mm the far-field approximation is valid. Consequently, the E-field distribution on the secondary mirror corresponds

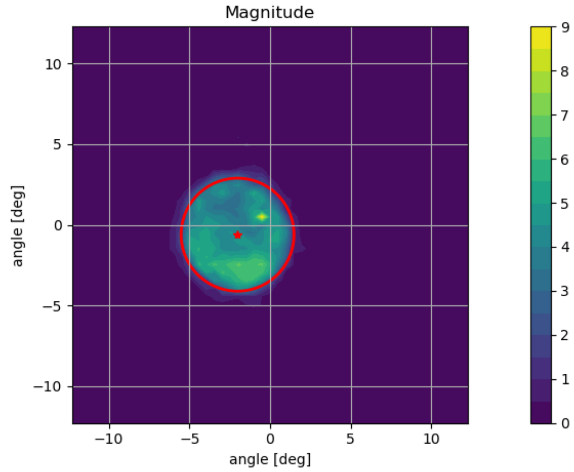

Fig. 8. Magnitude of E-Field distribution at telescope secondary mirror (arbitrary units). The red circle shows the subtended secondary position as seen from the measurement plane.

to the Fourier transform of the measured E-field. Fig. 8 shows the E-field magnitude at the secondary for the example measurement presented in Fig. 7.

A single scan allows the measurement of a small fraction of the complete AMKID focal plane, whose dimensions are 44 $\times$ 44 cm^2. Additionally, for this experiment we only have one KID read-out, while 4 read-out lines are required to read all the array information at 350 GHz. For the high frequency array, the situation is even more complicated as 20 read-out lines are required to process the complete array information. These two limitations imply that we have to repeat the measurement several times to cover a large fraction of the instrument focal plane. In this process, we are also limited by other instrumental constrains as the reachable area, the finite size of XY scanner, the already referred problems with reference illumination, problems with linearity due to background or excess signal, and also the presence of nonfunctional or defective detectors in the array. After selecting good quality data, we obtained the required information for 377 KIDs in an area of 35 $\times$ 30 cm^2. Due to the previously enumerated problems the sampling of the area was not uniform, but it is sufficient to offer a first glimpse of the instrument optical performance. In this article, specially focused on the experimental method, we present just the preliminary obtained results, which prove the power of the proposed characterization method. In a future instrument devoted article, we would report on the instrument performance, including other parameters beside optical quality.

A. *Beam Shape*

A relevant parameter for astronomical observations is the beam shape, usually characterized through the beam size and ellipticity. Using our measurements, we can do a first estimation of this parameter. The wave front at telescope aperture is forward propagated using Fourier optic and the expected beam shape on sky is obtained. It is important to notice here that all the discussion in this section consider a perfect telescope, which is not a realistic scenario, but a useful exercise to understand

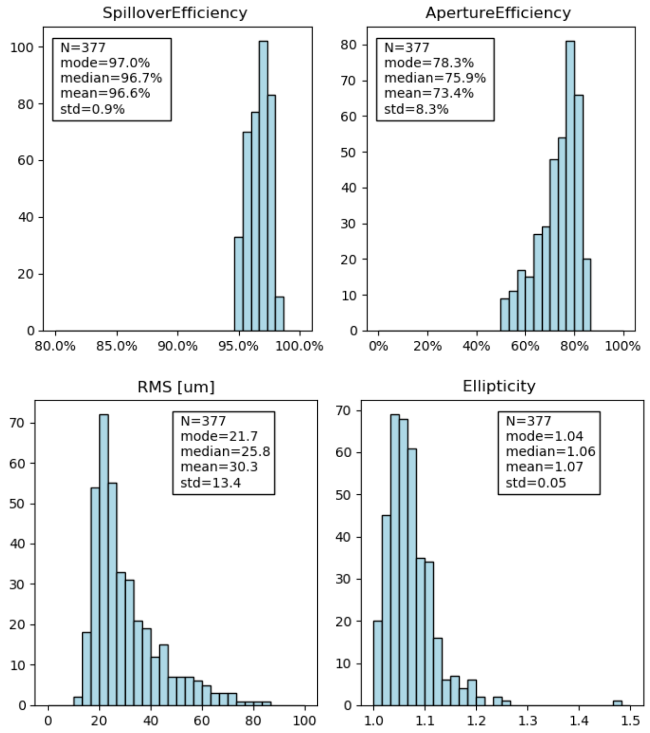

Fig. 9. Top, distribution of spill-over and aperture efficiency for the set of beams under analysis. Bottom, distribution of wavefront error and beam ellipticity for the set of beams under analysis.

the effect of the instrument optics on final performance. The obtained beam pattern on sky is fit by a Gaussian, and ellipticity computed as the ratio between the major and minor axis. Results indicate that beam shape on sky is $15.8' \pm 0.8'$, with an ellipticity lower than 1.2 on most of the sampled pixels, as presented in Fig. 9. As comparison we can say that simulated values for typical fields are beam sizes of $16.3' \pm 0.5'$, with ellipticity better than 1.1.

B. Aperture Efficiency

The aperture efficiency is the most important parameter on the system as it quantifies the coupling to a perfect point source. Experimentally it is measured as

$$\eta_{\text{aperture}} = \frac{\left|\int_{\text{secondary}} E_{co} d\Omega\right|^2}{\int_{all} |E_{tot}|^2 d\Omega} \tag{6}$$

where E_{co} is the copolar electric field pattern on the subreflector and E_{tot} is the total electric field, copolar plus cross-polar. The aperture efficiency can be expressed as the product of the spill-over efficiency, the amplitude efficiency, the phase efficiency, and the cross-polar efficiency, as defined in [20]. In our analysis, polarization efficiency is not considered and, therefore, is considered to be 1 for the data analysis. Amplitude and phase efficiency are a measure of how well the subreflector illumination resembles a perfect illumination, i.e., a flat-hat E-field distribution. Finally, the spill-over efficiency, of special relevance for optics in radio-astronomy telescopes, determines

TABLE I
LOW FREQUENCY ARRAY OPTIC EFFICIENCY

Measured values (N=377)				
	$\eta_{spillover}$	$\eta_{amplitude}$	η_{phase}	$\eta_{aperture}$
Mode	97%	88%	92%	78%
Median	97%	88%	90%	76%
Mean	97%	86%	88%	73%
Sigma	1%	5%	6%	8%
Simulated values (N=9), GRASP				
	$\eta_{spillover}$	$\eta_{amplitude}$	η_{phase}	$\eta_{aperture}$
Mean	99%	91%	96%	86%

how much power on the beam successfully reaches the subreflector. It is defined as

$$\eta_{\text{spillover}} = \frac{\int_{\text{secondary}} |E_{tot}|^2 d\Omega}{\int_{\text{all}} |E_{tot}|^2 d\Omega}. \tag{7}$$

It is important to highlight that the previously described efficiencies deal with optic parameters, other efficiency losses such as the quantum efficiency, or detector window losses are not considered in the discussion. In our sample, the aperture efficiency is determined to be 76%. Fig. 9 shows the typical distribution of parameters in the sample of KIDs we studied. It is seen that most of the distributions are asymmetric, and therefore, the median is considered a more suitable statistical descriptor than the mean. In Table I, the measured values of the system optical efficiencies are listed together with results from numeric simulations based in physical optics. The simulations were done using a commercial software (GRASP) over a selection of 9 fields at 350 GHz. In the simulations ideal surfaces were used along with a perfect alignment. The selection of fields included the 4 corners of the field of view, where degraded performance is expected. Therefore, the calculated mean value is slightly lower than a typical field. Results predicted an aperture efficiency of 86%, a value larger than the measured values 76%. This discrepancy can be explained by the additional errors introduced as a result of imperfect mirrors and alignment. The Ruze's equation

$$\eta_{\text{ruze}} = e^{-\left(\frac{4\pi\in}{\lambda}\right)^2} \tag{8}$$

is a measure of how much efficiency degradation we expect by using an imperfect reflector, characterized by its root mean square (rms) error, $\in$. It was found that the difference between measurement and simulation can be explained by a system of mirrors having an equivalent error of 24 μm rms error. This value is consistent with previous metrology measurement of mirrors, which indicate that mirror surfaces quality ranges between 7 and 17 μm rms.

C. Wavefront Distortion

As seen in previous discussion, the system under characterization is suspected to be degraded by imperfect mirrors surface and alignment. For this discussion, the concept of wavefront distortion is especially relevant, as it is equivalent to a direct measurement of the optical quality of the mirrors in the system under characterization. To calculate it, the measured electric field pattern at the secondary mirror is corrected to remove the

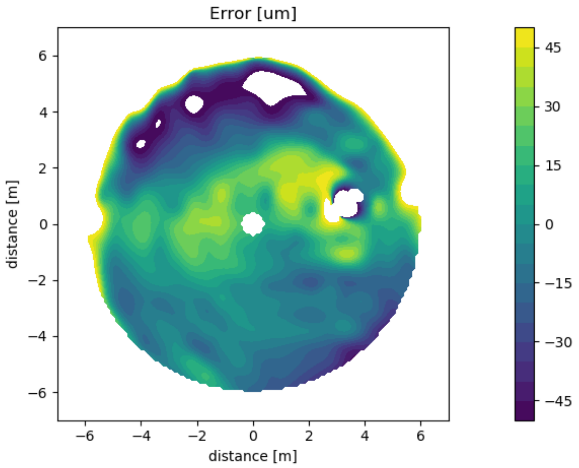

Fig. 10. Equivalent mirror surface accuracy calculated from beam under analysis in Fig. 6. It is a representation in which the wavefront error is presented as generated by a single defective mirror.

curvature and tilt terms arising from being out of focus and OFF-axis relative to the telescope optical axis. The results, known as wavefront error, is a measure of how much the wavefront at telescope aperture depart from a perfect flat wave. This wavefront error is converted to an equivalent surface accuracy projected on the telescope main aperture. Fig. 10 shows the result of this calculation for the specific set of data presented in Fig. 7. Results show an astigmatic component and high spatial frequency noise. Overall, a surface rms error of 26 μm was measured in that particular example. A more complete overview is presented in Fig. 9 where the histogram of the obtained rms value for different measurement points is shown. It can be observed that measured values in the range of 20–30 μm agrees with our previous estimation based on the loss of efficiency between simulations and measurements, an interesting point come from the fact that simulations pointed out that even a perfectly built system would have around 11 μm rms error. This is caused by the fact that getting a perfect performance over the complete field of view is not possible, and the system optimization yields a tradeoff solution for a weighted goal of fields across a manifold of fields. More details on the optic design strategy and results can be found in [11]. Anyway, as rms errors add quadratically, the design error contributes little to the measured values, meaning that mirror surface errors and misalignments in the optical system dominates the measured wavefront error.

VI. Extension to 850 GHz Band

One of the main advantages of photonic devices over their counterpart, solid-state multipliers, is their ability to operate over a larger frequency range without major changes in the experimental setup. In our case, the system can be tuned from around 100 GHz to 2 THz. To demonstrate this capability, and taking advantage of the dual color feature of the AMKID, the lasers were tuned to operate at 850 GHz and the system was used to characterize a single field (60 mm $\times$ 60 mm) of the high frequency array. In addition to the laser tuning, the amplitude of

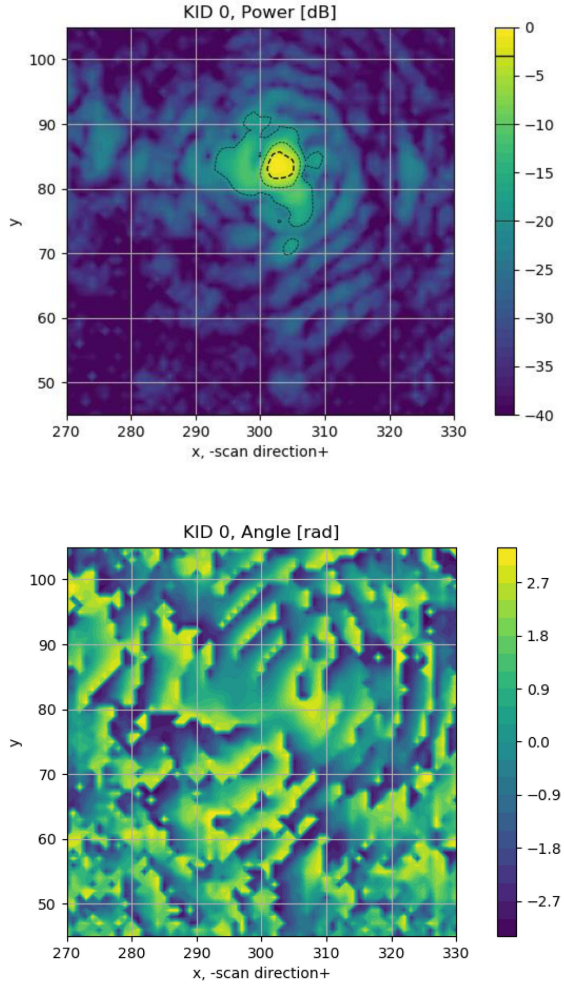

Fig. 11. Phase (bottom) and amplitude (top) beam map of a specific detector in the HFA. Measurement done at 850 GHz.

the saw-teeth signal was down-scaled by a factor three in order to obtain a similar phase modulation depth as in the 350 GHz case. The system could be retuned in little time and a set of data at 850 GHz was directly measured. The characterization system behaved similarly to the 350 GHz measurements, delivering an excellent SNR of more than 40 dB. Fig. 11 shows the measured phase and amplitude beam of a typical measured pixel in the center of the field.

In this experiment a set of around 10 pixels in the central area of the map were successfully measured. Results indicate that the on-sky beams have a halfwidth beam size of 7.2" with an ellipticity value of 1.15. The measured wavefront error in this area is in the range 14–18 μm, corresponding to a very good section of the focal plane, (compare to Fig. 9 for rms distribution as measured in previous section). Measured aperture efficiency in the range of 54% to 68%, are therefore, an upper value for the instrument. It is very important to recall that these results cannot be extended to the complete array, as we are just testing single positions. To complete the discussion about the expected 850 GHz performance it is possible to use the Ruze formula (8) to estimate the degradation of the array at high frequency. It is found that for an rms error of 20 μm the HFA will degrade by 65% as compared

to the LFA performance. But if we consider average areas of the focal plane, with wavefront errors of 26 μm, the degradation is 48%, presenting serious problems to efficient observations.

VII. Conclusion

In this article, a system for phase and amplitude measurement of large field of view bolometric instruments in the subterahertz regime is presented. This method uses photonic sources providing a huge flexibility on the frequency coverage, reducing the size and complexity of the system when compared to the use of solid-state sources. A clear advantage of photonic sources is the ability to generate signals in the terahertz regime, which is neither cost effective nor straightforward with solid-state sources. The high power delivered by solid-state devices, operating in the low terahertz regime, is in this case not an advantage, as detector saturation is one of the main issues when measuring sensitive detectors systems. The main advantage of solid-state sources over photonic devices is the availability of well calibrated probes and horns to generate the required clean illumination pattern. In our case, this issue was solved by using a small aperture to clean the source beam, and by modifying one of the sources to achieve the required beamwidth. More advanced solutions can be implemented on this regard.

As an application for this technique, we have presented the results of a measurement campaign towards a complete characterization of a dual color high field of view KID based instrument for the APEX telescope (AMKID). Results indicate an optical quality of the instrument characterized by a half wavefront error of in the range from 20 to 30 μm rms. This value is sufficient for observations in the 350 GHz band, but imposes limitations in the 850 GHz band. Motivated by this work, we are currently working on improving mirror quality to gain observation efficiency in the higher frequency band. Presented results give an accurate prediction of the system performance in laboratory environment, including errors in the optic, detectors, and design limitations. Final measurement, after on-site deployment, will also include telescope associated errors. Therefore, a complete laboratory characterization is a fundamental step to understand instrument performance, decoupling it from telescope effects. In this context, we remark that systems based in photonic sources are a versatile tool for laboratory characterization of large focal plane array instruments. In particular for instrument that have several frequency bands, where a single test system can be used to characterize the complete instrument.

Acknowledgment

The authors would like to thank the complete AMKID team at MPIfR and SRON for support and useful discussions, especially H. Hoevers, C. Heiter, A. Schmitz, A. Goerlitz, A. Kovacs, and S. Jorquera, like to thank I. Veenendaal, E. Castillo, and W. Jellema, for useful discussions on experimental techniques, and also D. Thoen and V. Murugesan for array fabrication.

References

[1] P. Klaseen et al., "The Atacama large aperture submillimeter telescope (AtLAST)," in *Proc. SPIE Astronomical Telescopes + Instrum., Ground-Based Airborne Telescopes VIII*, 2020, Art. no. 114452F.

[2] CCAT-Prime collaboration, "CCAT-prime collaboration: Science goals and forecasts with prime-cam on the fred young submillimeter telescope," *Astrophysical J. Suppl. Ser.*, vol. 264, no. 7, Jan. 2023, Art. no. 39.

[3] P. Day et al., "A broadband superconducting detector suitable for use in large arrays," *Nature*, vol. 425, no. 6960, pp. 817–821, Oct. 2003.

[4] J. J. A. Baselmans et al., "A kilo-pixel imaging system for future space based far-infrared observatories using microwave kinetic inductance detectors," *Astron. Astrophys.*, vol. 601, 2016, Art. no. 29653.

[5] R. M. J. Janssen et al., "High optical efficiency and photon noise limited sensitivity of microwave kinetic inductance detectors using phase readout," *Appl. Phys. Lett.*, vol. 103, no. 20, 2013, Art. no. 203503.

[6] R. Adam et al., "The NIKA2 large-field of view millimetre continuum camera for the 30 m IRAM telescope," *Astron. Astrophys.*, vol. 609, Jan. 2018, Art. no. A115.

[7] E. Castillo-Dominguez et al., "Mexico-U.K. sub-millimeter camera for astronomy," *J. Low Temp. Phys.*, vol. 193, Jul. 2018, Art. no. 1010.

[8] I. Lowe et al., "Characterization, deployment, and in-flight performance of the BLAST-TNG cryogenic receiver," *Proc. SPIE*, vol. 11453, 2020, Art. no. 1145304.

[9] J. E. Austermann et al., "Millimeter wave polarimeters using kinetic inductance detectors for TolTEC and beyond," *J. Low Temp. Phys.*, vol. 193, pp. 120–127, May 2018.

[10] R. Güsten et al., "The Atacama pathfinder experiment (APEX), a new submillimeter facility for southern skies," *Astron. Astrophys.*, vol. 454, no. 2, pp. L13–L16, 2006.

[11] L. Esteras, "The optical system and the astronomical potential of A-MKID, a new camera using microwave kinetic inductance detector technology," Ph.D. dissertation, Univ. of Bonn, Bonn, Germany, 2014.

[12] D. Moinard, S. Withington, and C. N. Thomas, "Probing infrared detectors through energy-absorption interferometry," in *Infrared Sensors, Devices, and Applications VII*, P. D. LeVan, A. K. Sood, P. Wijewarna-suriya, and A. I. D'Souza, Eds. Bellingham, WA, USA: SPIE, Aug. 2017, Art. no. 22.

[13] K. K. Davis et al., "Complex field mapping of large direct detector focal plane arrays," *IEEE Trans. Terahertz Sci. Technol.*, vol. 9, no. 1, pp. 67–77, Jan. 2019.

[14] S. J. C. Yates et al., "Complex beam mapping and Fourier optics analysis of a wide-field microwave kinetic inductance detector camera," *J. Low Temp. Phys.*, vol. 199, pp. 156–163, 2020.

[15] A. Murphy et al., "Multi-mode horn design and beam characteristics for the Planck satellite," *J. Instrum.*, vol. 5, no. 4, 2010, Art. no. T04001.

[16] I. Cámara Mayorga et al., "Terahertz photonic mixers as local oscillators for hot electron bolometer and superconductor-insulator-superconductor astronomical receivers," *J. Appl. Phys.*, vol. 100, no. 4, 2006, Art. no. 043116.

[17] I. C. Mayorga, A. Schmitz, T. Klein, C. Leinz, and R. Gusten, "First in-field application of a full photonic local oscillator to terahertz astronomy," *IEEE Trans. Terahertz Sci. Technol.*, vol. 2, no. 4, pp. 393–399, Jul. 2012.

[18] P. de Groot, "Phase shifting interferometry," in *Optical Measurement of Surface Topography*. Berlin, Germany: Springer, 2011.

[19] G. Grutzeck et al., "A MKID-readout based on a heterogeneous, closely coupled architecture," in *Proc. 32th Int. Symp. Space Terahertz Technol.*, 2022.

[20] S. B. Sørensen and K. Pontoppidan, "Analysis of the ALMA telescope and front-ends," in *Proc. 21st Int. Symp. Space Terahertz Technol.*, 2010, pp. 121–127.